photonics

MDPI

Article

Plastic Scintillating Fiber Mesh Array Detector for Two-Dimensional Gamma-Ray Source Localization Using an Artificial Neural Network

Jinhong Kim [1], Sangjun Lee [1], Jae Hyung Park [1], Seunghyeon Kim [1], Seung Hyun Cho [2], Chulhaeng Huh [3] and Bongsoo Lee [1,*]

[1] School of Energy Systems Engineering, Chung-Ang University, Seoul 06974, Republic of Korea; kenaz93@cau.ac.kr (J.K.); gkdlsjfl@cau.ac.kr (S.L.); sksdoe@cau.ac.kr (J.H.P.); sjss555@cau.ac.kr (S.K.)
[2] Department of Materials Science and Engineering, Soong-Sil University, Seoul 06978, Republic of Korea; scho@ssu.ac.kr
[3] Department of Radiation Oncology, Augusta University, Augusta, GA 30912, USA; chuh@augusta.edu
* Correspondence: bslee@cau.ac.kr

Abstract

In this study, a two-dimensional gamma-ray source localization system using a mesh array of plastic scintillating fibers and an artificial neural network is presented. The system covers a 200 cm by 100 cm area using SCSF-78 multi-cladded fibers. A novel U-shaped fiber topology connects both fiber ends to one side, requiring only two data-acquisition systems. Silicon photomultiplier arrays measure fast time-of-flight under optimized operating conditions to maximize signal yield. An independent artificial neural network model map measured time-of-flight values to spatial coordinates, compensating for systematic non idealities. Performance was validated using a Cesium-137 source at 20 random test positions. The artificial neural network method achieved a mean full-scale error of 4.6%. This demonstrated a 79.34% accuracy improvement over direct theoretical calculation, which had a mean full-scale error of 22.5%. The system showed consistent performance, achieving a two-dimensional standard deviation of 0.492 cm during repeatability assessment. This methodology provides a practical, efficient approach to two-dimensional radiation source localization suitable for real time monitoring and contamination mapping.

Keywords: plastic scintillating fiber; artificial neural network; 2-dimensional radionuclide localization; optical sensor; fiber mesh array

check for updates

Received: 12 November 2025
Revised: 28 November 2025
Accepted: 11 December 2025
Published: 12 December 2025

Citation: Kim, J.; Lee, S.; Park, J.H.; Kim, S.; Cho, S.H.; Huh, C.; Lee, B. Plastic Scintillating Fiber Mesh Array Detector for Two-Dimensional Gamma-Ray Source Localization Using an Artificial Neural Network. *Photonics* **2025**, *12*, 1227. https://doi.org/10.3390/photonics12121227

Copyright: © 2025 by the authors. Licensee MDPI, Basel, Switzerland. This article is an open access article distributed under the terms and conditions of the Creative Commons Attribution (CC BY) license (https://creativecommons.org/licenses/by/4.0/).

1. Introduction

The importance of radiation monitoring systems has been underscored by major nuclear accidents throughout history. The Chernobyl disaster in 1986 and the Fukushima Daiichi accident in 2011 demonstrated that the severity of nuclear incidents is primarily determined not by internal facility damage, but by the extent of radioactive material released into the environment [1,2]. The International Nuclear and Radiological Event Scale (INES) classifies these events largely based on off-site radiological consequences and environmental contamination levels [3]. These incidents emphasized the critical need for rapid, accurate radiation detection and source localization capabilities to enable timely emergency response and protect public health.

Beyond emergency scenarios, continuous radiation monitoring serves essential functions in peacetime operations. Nuclear power plants require routine contamination surveys

to detect potential leaks or abnormal radiation levels. Medical facilities using radiopharmaceuticals and radiotherapy equipment need monitoring to ensure safe working environments. Industrial applications involving radioactive sources, research laboratories handling radioactive materials, and border security operations all demand reliable radiation detection systems [4,5]. The ability to not only detect radiation but also accurately determine the spatial location of sources significantly enhances the effectiveness of these monitoring programs.

Conventional radiation monitoring approaches typically employ point detectors distributed across an area, providing surveillance through networked sensor arrays. While effective for broad-area coverage, these systems often lack the spatial resolution needed for precise source localization, particularly in scenarios requiring rapid identification of contamination distributions or multiple source locations. Technologies capable of providing detailed spatial mapping with high temporal resolution offer complementary capabilities that can improve monitoring effectiveness.

Plastic scintillating fiber (PSF) technology presents unique advantages for radiation detection applications. The flexible geometry of PSF allows conformance to various surfaces and measurement configurations, enabling deployment in diverse environments including curved surfaces, tight spaces, and irregular geometries where rigid detectors cannot be installed [6,7]. The continuous sensitivity along the fiber length provides coverage of extended areas without gaps, unlike discrete point detectors that leave unmonitored regions between sensors. PSF exhibits fast timing response with decay times typically in the nanosecond range, making it suitable for time-of-flight (ToF) measurements and high count-rate applications. Additionally, PSF systems offer relatively low cost compared to inorganic scintillator arrays or semiconductor detector systems, particularly when covering large areas [8,9].

The operational principle of PSF-based detection relies fundamentally on optical phenomena. When ionizing radiation interacts with the plastic scintillator material, energy is deposited through Compton scattering or photoelectric absorption, exciting fluorescent molecules within the polymer matrix. These molecules subsequently emit optical photons in the blue spectral region, typically with peak wavelength around 420–450 nm. The scintillation photons are guided along the fiber through total internal reflection at the core-cladding interface, with the multi-clad structure providing enhanced light collection efficiency. The optical signal propagates bidirectionally toward both fiber ends at a velocity determined by the refractive index of the core material, typically around 1.58–1.60 for polystyrene-based scintillators. The difference in ToF between photon arrival at the two fiber ends encodes spatial information about the interaction location. This optical timing measurement forms the basis for position-sensitive detection, transforming the PSF into a distributed radiation sensor with continuous spatial sensitivity. The photon detection efficiency, timing resolution, and dynamic range of the photodetectors directly influence the achievable position accuracy, making the optical readout system a critical component of the localization performance.

However, PSF-based detection systems face certain challenges that limit their performance. The light output of plastic scintillators is generally lower than that of inorganic scintillators such as NaI(Tl) or BGO, resulting in reduced energy resolution and potentially lower detection efficiency for low-energy gamma rays [5]. Light attenuation along extended fiber lengths causes position-dependent signal amplitudes, with interactions occurring far from photodetectors producing weaker signals that may fall below detection thresholds. The timing characteristics of scintillation light propagation can be affected by various factors including fiber bending, temperature variations, and mechanical stress, introducing systematic uncertainties in ToF measurements. Furthermore, the relationship

between measured timing distributions and source positions can be complex, particularly in multi-fiber array configurations where multiple detection events and geometric effects make direct analytical position calculation difficult or inaccurate.

Artificial intelligence techniques, particularly artificial neural networks (ANNs), offer powerful approaches to address these challenges in PSF-based radiation detection. ANNs can learn complex, non-linear relationships between measured signals and physical parameters without requiring explicit analytical models of all contributing factors [10,11]. For radiation source localization, ANNs can be trained to map measured detector responses—including ToF distributions, signal amplitudes, and event patterns—to spatial coordinates. This approach effectively learns the inverse problem of inferring source position from detector data, automatically accounting for systematic effects such as light attenuation, timing offsets between channels, detector response variations, and geometric dependencies. The ability of ANNs to extract position information from complex, noisy data distributions has been demonstrated in certain radiation detection applications [12,13].

Our previous work established the feasibility of one-dimensional (1D) gamma-ray source localization using PSF technology combined with ToF measurements and ANN analysis [14]. In that study, scintillation light generated by gamma-ray interactions in the fiber propagated to both fiber ends, where the arrival time difference provided position information along the fiber axis. An ANN trained on systematic calibration data achieved position estimation accuracy significantly superior to theoretical calculations based on measured time differences, demonstrating the value of ANNs in compensating for systematic measurement effects.

Extending localization capability from one dimension to two dimensions is essential for practical radiation monitoring scenarios where spatial distributions across areas must be characterized rather than along linear paths. Two-dimensional (2D) coverage enables applications including contamination mapping over floor surfaces, area surveys following radiological incidents, monitoring of large equipment or facility sections, and simultaneous tracking of multiple radiation sources. An efficient approach involves arranging fibers in a mesh configuration with U-shaped paths where both fiber ends connect to the same readout electronics, substantially reducing required hardware while maintaining complete 2D coverage through perpendicular fiber orientations.

Silicon photomultiplier (SiPM) arrays have emerged as attractive photodetectors for scintillation light measurement in PSF systems. As solid-state photon counting devices, SiPMs consist of arrays of silicon avalanche photodiodes operated in Geiger mode, each functioning as an independent photon detector. When an optical photon is absorbed in silicon, it generates an electron-hole pair that triggers an avalanche multiplication process, producing a measurable electrical pulse. The fast avalanche development and quenching dynamics enable superior timing resolution compared to conventional photomultiplier tubes (PMTs), with single-photon timing resolution below 100 ps enabling precise optical ToF measurements [15,16]. The photon detection efficiency, defined as the probability of detecting an incident photon, directly impacts the signal-to-noise ratio in low-light detection scenarios typical of PSF applications. The compact solid-state construction eliminates fragile glass envelopes and high-voltage requirements, while insensitivity to magnetic fields allows operation in environments where conventional PMTs cannot function. Recent advances have produced SiPM devices with high photon detection efficiency in the blue spectral region matching PSF emission, large active areas suitable for coupling to scintillating fibers, and low dark count rates enabling detection of weak optical signals [17].

This paper presents a 2D gamma-ray source localization system employing a fixed mesh-based array of PSFs with U-shaped topology, SiPM array readout, and ANN-based position estimation. Specifically, this study focuses on surface contamination monitor-

ing applications, validating the localization methodology for a single dominant radioactive source positioned on the detector plane. The system covers a measurement area of 200 cm × 100 cm (2.0 m^2) using fibers oriented in two perpendicular directions. The key contributions of this work include the demonstration of an efficient U-shaped fiber topology that enables one readout per spatial axis, requiring only two data acquisition systems for complete 2D coverage. We present systematic optimization of SiPM operating parameters and identify an anomalous noise phenomenon occurring within a specific time-over-threshold (ToT) range. Independent ANN models are developed and validated for 2D position estimation using ToF measurements in both spatial dimensions. Comprehensive performance evaluation across random test positions demonstrates significant improvement in localization accuracy compared to theoretical calculation methods.

2. Materials and Methods

The PSF selected for this study was SCSF-78 manufactured by Kuraray Co., Ltd., Tokyo, Japan, which is a multi-cladded PSF with specifications optimized for long-distance light transmission. The fiber has a diameter of 2.0 mm and features a multi-cladding structure with core refractive index of 1.59, providing efficient light guiding through total internal reflection at the core-cladding interfaces. The scintillation emission spectrum peaks at 450 nm wavelength, well-matched to the spectral sensitivity of silicon-based photodetectors. The decay time of 2.8 ns enables fast timing response suitable for ToF measurements. Importantly, the attenuation length of 4.0 m allows deployment of extended fiber lengths while maintaining adequate signal strength at the photodetectors [7].

The mesh-based sensor array was configured to cover a measurement area of 200 cm × 100 cm, providing total coverage of 2.0 m^2. Multiple PSF strands were arranged in a grid pattern with fibers oriented in two perpendicular directions. One set of fibers provided sensitivity along the *X*-axis direction spanning 200 cm, while the perpendicular set provided sensitivity along the *Y*-axis direction spanning 100 cm. Each individual fiber was physically formed into a U-shape where the fiber extends in one direction within the measurement area, curves around outside the measurement area boundary, and returns along a parallel path. Both ends of each U-shaped fiber are terminated on the same side of the measurement area, enabling connection to a single data acquisition unit. The straight portions of the fiber within the measurement area constitute the active detection region with continuous sensitivity to radiation interactions, while the curved portion outside the measurement area simply routes the fiber back to the readout side without contributing to detection. Figure 1 illustrates part of system configuration showing the mesh pattern, U-shaped fiber paths, and connection to DAQs.

To facilitate a clear understanding of the system operation, the complete signal processing chain is illustrated in Figure 2. The workflow proceeds from photon generation in the U-shaped fibers to SiPM detection, digitization, peak selection, and finally, position estimation via the ANN model.

This U-shaped fiber topology provides several practical advantages for system implementation. Both ends of each fiber connect to channels on the same data acquisition board, eliminating the need for separate readout electronics on opposite sides of the measurement area. One data acquisition unit handled all *Y*-axis fibers, while a second unit handled all *X*-axis fibers, enabling complete 2D coverage using only two data acquisition systems.

When a gamma-ray interaction occurs within the measurement area, scintillation light is generated at the interaction point and propagates bidirectionally along the fiber toward both ends. The optical ToF difference between photon arrivals at the two fiber ends encodes the position of the interaction along that fiber axis. The combination of measurements from the two perpendicular fiber sets enables 2D position determination.

In cases where a source is positioned between multiple parallel fibers, adjacent fibers may detect the radiation simultaneously, resulting in multiple peaks in the time difference histogram. Additionally, due to the U-shaped topology, a single fiber traversing the area twice can generate distinct peaks if the source interacts with both legs. To handle this, we employed a dominant signal selection strategy. The ANN architecture utilized in this study requires a fixed input dimension. Incorporating variable numbers of secondary peaks would introduce complexity and ambiguity to the input features. Therefore, we selected only the peak with the highest count rate (the dominant channel) for position estimation. This approach ensures that the ANN receives a consistent and statistically robust input feature corresponding to the primary interaction point, thereby stabilizing the model performance.

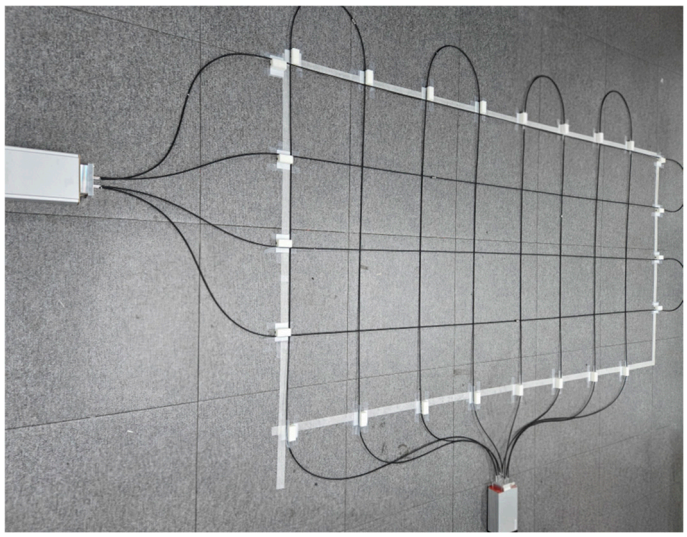


Figure 1. Sensor configuration including the connection to DAQs.

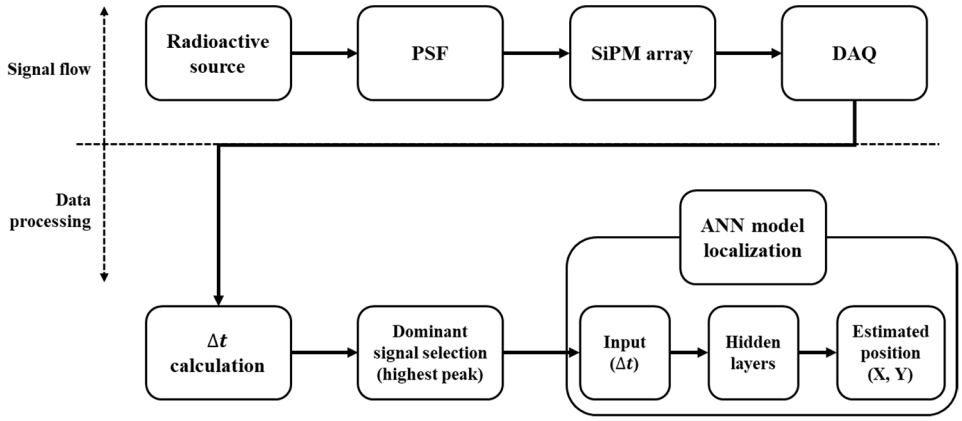


Figure 2. Entire workflow for 2D localization.

For scintillation light detection at fiber ends, ARRAYJ-60035-64P-PCB silicon photomultiplier arrays manufactured by SensL Technologies, Cork, Ireland (now part of onsemi) were employed. Each array consists of an 8 × 8 arrangement of 64 individual SiPM elements. Each element measures 6.13 mm × 6.13 mm, providing total active area of 50.44 mm × 50.44 mm per array including approximately 0.2 mm gaps between elements. The breakdown voltage is 24.2 V minimum. The photon detection efficiency reaches maximum values in the blue spectral region around 420 nm, matching the emission spectrum of SCSF-78 [18]. Optical coupling between fiber ends and SiPM arrays was achieved through

SMA connectors for fiber termination combined with custom metal connectors fabricated to ensure proper alignment and light-tight coupling between fiber ends and SiPM active areas.

The two ends of each fiber were connected to two different channels of the 64-channel SiPM array. The channel assignments were designed to maintain spacing between fibers to minimize optical crosstalk between adjacent SiPM channels. With 64 channels available per SiPM array, up to 32 fibers could theoretically be connected to a single digitizer. However, to ensure adequate channel separation and avoid crosstalk, not all available channels were utilized, and fibers were connected with spacing between their assigned channel pairs.

The data acquisition system employed DT5202 desktop digitizers manufactured by CAEN S.p.A., Viareggio, Italy. Key specifications include 5 GS/s sampling rate, 12-bit resolution, and 16 input channels per digitizer unit. The digitizer extracts timing and amplitude information from detected pulses, outputting channel number, timestamp with 20 ps resolution, time-of-arrival, pulse amplitude, and ToT for each detected event. To mitigate gain variations caused by ambient temperature fluctuations, the digitizer's internal active temperature compensation mechanism was enabled. This feature continuously monitors the probe temperature and automatically adjusts the SiPM bias voltage based on the manufacturer-specified temperature coefficient, ensuring stable detector response throughout the measurements [19]. Two DT5202 digitizers were deployed, one for *X*-axis fibers and one for *Y*-axis fibers.

Synchronization between the two digitizers was achieved using a DT5215 data concentrator module manufactured by CAEN S.p.A., Italy. The concentrator distributes a common master clock to both DT5202 units, aggregates data streams from both digitizers, and maintains a global timestamp counter enabling sub-nanosecond precision time correlation between events from the two digitizers [20].

Sealed gamma-ray sources were employed for system training and performance evaluation. For training data acquisition, a Co-60 source with activity of 24.4 μCi emitting 1.17 MeV and 1.33 MeV gamma rays was used. For test measurements, a Cs-137 source with activity of 37.1 μCi emitting 662 keV gamma rays was employed.

A 2D Cartesian coordinate system was established to describe source positions within the measurement area. The *X*-axis spans from 0 to 200 cm and the *Y*-axis spans from 0 to 100 cm, with each axis aligned to its respective fiber orientation. The origin at coordinates (X = 0 cm, Y = 0 cm) is positioned at one corner of the measurement area.

For all experimental measurements, including training and test datasets, the radioactive sources were placed directly on the detector plane. This setup was chosen to simulate a surface contamination monitoring scenario, which is the primary scope of this study. While the X and Y coordinates varied across the measurement area (including both on-fiber and inter-fiber gap positions), the vertical distance was maintained at zero to evaluate the system's intrinsic localization performance on the surface.

Training data were acquired systematically across a regular grid spanning the measurement area with positions spaced 25 cm apart in both X and Y directions, resulting in approximately 45 training positions. At each position, the Co-60 source was placed with positioning accuracy of approximately ±0.5 cm, and data were acquired continuously for 30 s.

Test data were acquired at 20 random positions distributed throughout the measurement area, specifically selected to fall between the training grid points to evaluate interpolation capability. At each test position, the Cs-137 source was placed with positioning accuracy of ±0.5 cm, and data were acquired continuously for 15 s. Additionally, repeatability was assessed through nine repeated measurements at a fixed position (95 cm, 45 cm), with the source removed and repositioned between measurements.

Position estimation along each axis relies on ToF measurements between the two ends of a fiber. For a U-shaped fiber with both ends at the same location but detecting light that propagated along the fiber in opposite directions, the time difference between arrivals at the two SiPM channels encodes the position where the gamma-ray interaction occurred. Consider a fiber segment of length L where scintillation light is generated at position x measured from one reference end. Light propagates toward both ends at velocity c/n, where c is the speed of light in vacuum and n is the refractive index of the fiber core material. For SCSF-78, the refractive index n = 1.59. The time difference between far end and near end arrivals is given by:

$$\text{ToF} = t_{\text{far}} - t_{\text{near}} = \left[\frac{(L-x)n}{c}\right] - \left[\frac{xn}{c}\right] = \frac{(L-2x)n}{c} \quad (1)$$

Solving for position x yields the theoretical position:

$$x = \frac{L}{2} - \frac{c \times \text{ToF}}{2n} \quad (2)$$

This equation provides a direct theoretical relationship between measured time difference and interaction position. However, in practice, several factors introduce deviations from this ideal relationship including timing offsets between channels due to cable length differences or electronics delays, light attenuation along the fiber causing position-dependent signal amplitudes affecting timing precision, channel-to-channel variations in SiPM response and digitizer characteristics introducing systematic position-dependent biases, finite timing resolution limiting position accuracy, and statistical variations in photon detection and electronic noise contributing random uncertainty. Due to these effects, theoretical calculation using Equation (2) typically yields position errors.

ANNs can learn to compensate for systematic deviations and optimize position estimation despite measurement non-idealities. Independent neural network models were developed for X-axis and Y-axis position estimation, with each model accepting ToF values as input and producing position coordinates as output.

The network architecture for both X and Y models consists of an input layer with one neuron corresponding to the ToF value in nanoseconds, two hidden layers with 200 neurons each using rectified linear unit (ReLU) activation functions, which provides non-linear transformation capability, and an output layer with one neuron producing the estimated position coordinate in centimeters. This architecture was selected based on successful results in our previous 1D localization study [14]. Dropout regularization at 50% rate was applied during training to prevent overfitting by randomly deactivating neurons, forcing the network to learn robust features rather than memorizing training examples.

Training both networks employed the Adam optimizer which adaptively adjusts learning rates for each parameter based on estimates of first and second moments of the gradients [21]. The loss function is mean-squared-error, appropriate for regression tasks where the objective is to minimize the squared difference between predicted and true positions. Training data were randomly split with 90% used for training and 10% reserved for validation monitoring to detect overfitting. Batch size was 64 samples per mini-batch. Early stopping terminated training if validation loss failed to improve for 5 consecutive epochs, preventing overfitting while allowing sufficient training time. Maximum training was set to 200 epochs though early stopping typically terminated training earlier.

Following the methodology established in our previous work [14], two-stage training with weighted correction was employed to systematically reduce position-dependent biases. In stage 1, the network was trained on the original ToF features and true positions from the training dataset. The trained network was then evaluated on the training dataset to

identify position-dependent systematic errors by comparing predicted positions to known true positions. In stage 2, correction weights representing systematic bias at each training position were calculated based on the stage 1 errors. Modified training labels were created by subtracting the correction weights from true positions, effectively pre-compensating for the systematic biases. The network was retrained using these modified labels. This approach systematically reduces position-dependent biases, improving accuracy beyond initial training by explicitly addressing systematic measurement effects that cannot be fully captured in the first training stage.

The neural networks were implemented using Keras (v2.10.0) with TensorFlow (v2.10.1) backend in Python (v3.9.23). Training was performed on GPU, sufficient for the network sizes and dataset scales in this study. Trained models were saved for deployment in position estimation during test measurements.

For each test measurement, ToF values were extracted from detected events after filtering based on amplitude thresholds to reject noise and time discriminator (TD) thresholds set according to optimized parameters. Valid ToF values were input to the trained neural networks, with the *X*-axis network producing X-coordinate estimates and the *Y*-axis network producing Y-coordinate estimates.

Performance evaluation compared the estimated positions against known true positions. For each test position, the positioning error was quantified using the Full-Scale Error (FSE) based on the Euclidean distance between the estimated and true coordinates. This method normalizes the absolute positioning error relative to the maximum possible deviation within the measured area. The FSE is calculated by dividing the 2D Euclidean distance by the diagonal length of the measured area:

$$FSE\ (\%) = \frac{\sqrt{(x_{\text{true}} - x_{\text{estimated}})^2 + (y_{\text{true}} - y_{\text{estimated}})^2}}{\sqrt{(Range_x)^2 + (Range_y)^2}} \times 100 \tag{3}$$

where (x_{true}, y_{true}) denote the true source coordinates, and $(x_{estimated}, y_{estimated})$ are the positions estimated by the system. $Range_x$ and $Range_y$ represent the dimensions of the measurement area along the X and Y axes, respectively.

Additionally, the accuracy improvement rate was calculated comparing ANN-based estimation to theoretical calculation using:

$$\text{Improvement rate}\ (\%) = \frac{\text{FSE}_{\text{theory}} - \text{FSE}_{\text{ANN}}}{\text{FSE}_{\text{theory}}} \times 100 \tag{4}$$

where FSE_{theory} corresponds to the error derived from the theoretical calculation (Equation (2)), and FSE_{ANN} represents the error achieved by the proposed ANN model.

This quantifies the percentage reduction in position error achieved by the neural network compared to direct theoretical calculation from measured time differences, demonstrating the value of the ANN approach in compensating for systematic measurement effects.

3. Results

Systematic optimization of SiPM bias voltage and TD threshold parameters was conducted to establish operating conditions suitable for neural network training and position estimation. The bias voltage applied to the SiPM arrays was varied while maintaining a fixed Co-60 source position. For each voltage setting, data were acquired and the quality of timing signals was evaluated using the ratio of events contributing to the time difference histogram peak relative to total valid events.

Figure 3 shows time difference histograms for various bias voltage settings. At voltages from 26.0 V to 27.0 V, histograms exhibit identifiable peaks centered at the expected time difference corresponding to the source position, while the peak count increases significantly, maximizing signal yield. At 27.7 V and above, the rate of valid reconstructed events declines rapidly. While the raw trigger rate increases due to higher gain, the excessive electronic noise and dark counts result in a high rejection rate during data processing, leading to a drop in the usable signal throughput. Based on these observations combined with Table 1 data, 27.0 V was selected as the operating voltage, as it provided the maximum absolute peak count of 1348 events.

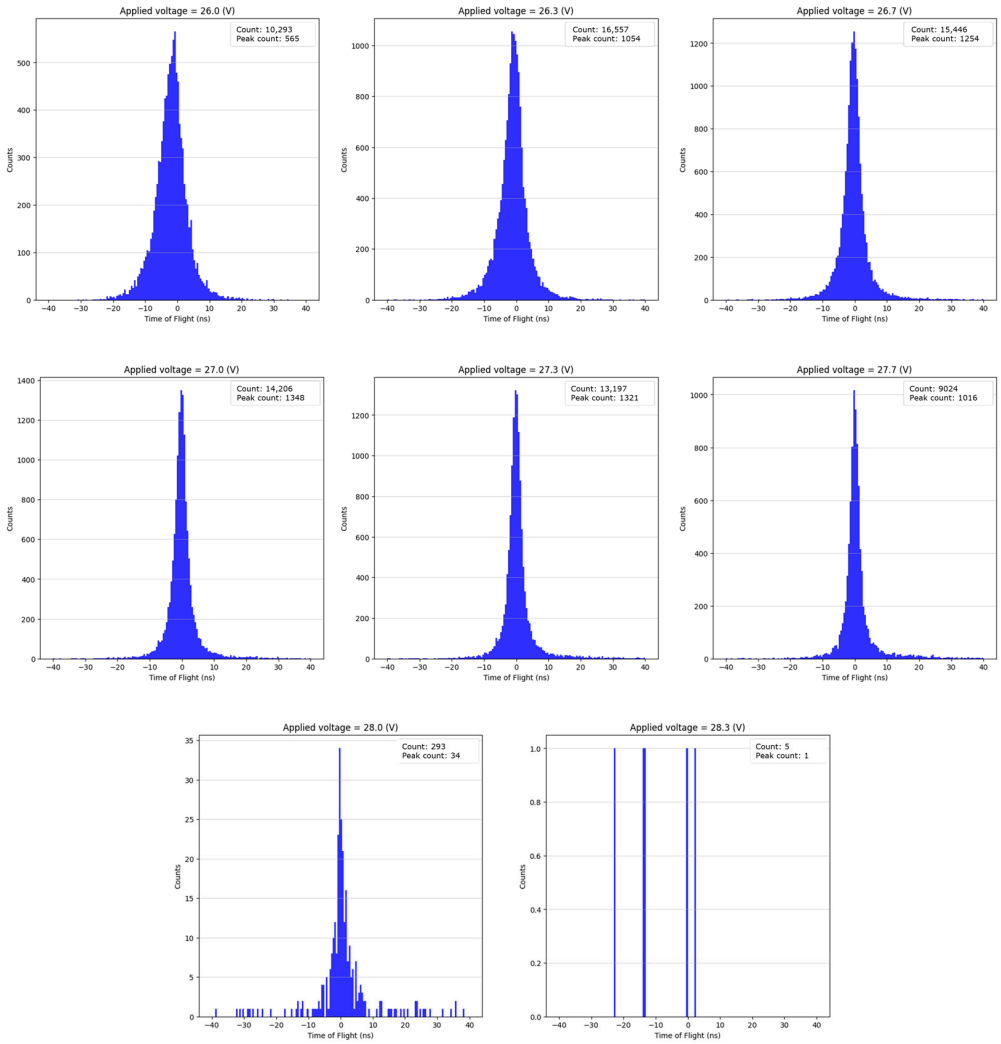


Figure 3. Effects of applied voltage variation on ToF histogram profiles.

Table 1. Performance metrics of the detection system as a function of applied bias voltage.

Applied Voltage (V)	Total Valid Events	Peak Count	Peak-Signal Ratio
26.0	10,293	565	0.052
26.3	16,557	1054	0.060
26.7	15,446	1254	0.075
27.0	14,206	1348	0.087
27.3	13,197	1321	0.091
27.7	9024	1016	0.101
28.0	293	34	0.104
28.3	5	1	0.167

The TD threshold parameter was investigated by acquiring data at a fixed source position and an optimized bias voltage of 27.0 V. The analysis threshold was set at 300 arbitrary digital units (ADU) to ensure stable operation of the acquisition system, thus avoiding the known instability region of the DAQ.

As the TD threshold is progressively raised from 300 ADU, Figure 4 confirms that the distinct signal peak structure remains largely stable up to an intermediate threshold, while the overall event rate consistently decreases. This inverse, non-linear relationship is quantified in Figure 5, which plots both the Total Event Count and the Peak Count as a function of the TD threshold. Both metrics decrease monotonically as the threshold increases. Exceeding an intermediate threshold value initiates a rapid and significant decline, indicating the progressive exclusion of valid, lower-amplitude scintillation pulses and subsequent statistical inefficiency.

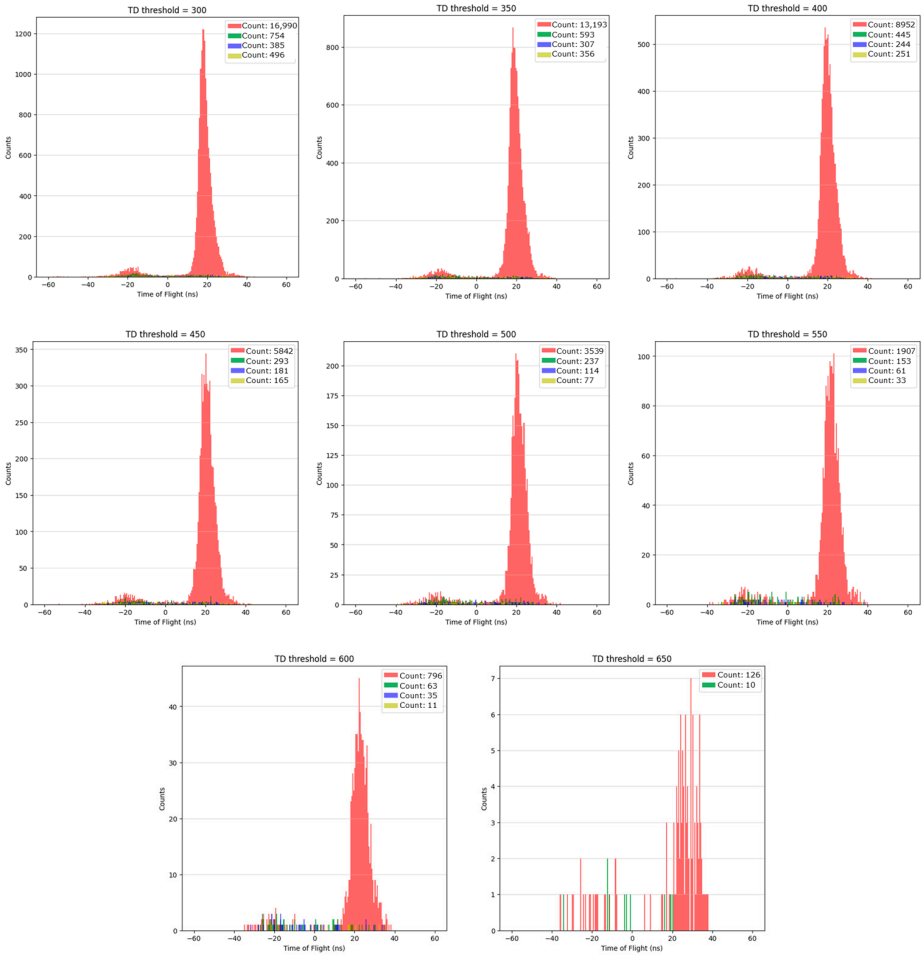


Figure 4. Effects of TD threshold variation on ToF histogram profiles. The different colors represent data from individual sensors.

To validate the impact of threshold selection on signal quality, we compared the ToF histograms obtained at 0 ADU and 300 ADU. As shown in Figure 6, the histogram at 300 ADU exhibits a significantly sharper peak with a narrower Full Width at Half Maximum compared to the 0 ADU setting. This confirms that a threshold of 300 ADU effectively filters out baseline noise that would otherwise degrade timing precision. Consequently, a TD threshold of 300 ADU was selected as the optimal operating point. This value was empirically determined to satisfy two critical conditions which are ensuring system stability by avoiding the instrumental instability region observed at lower thresholds and maximizing timing precision by rejecting the baseline noise floor.

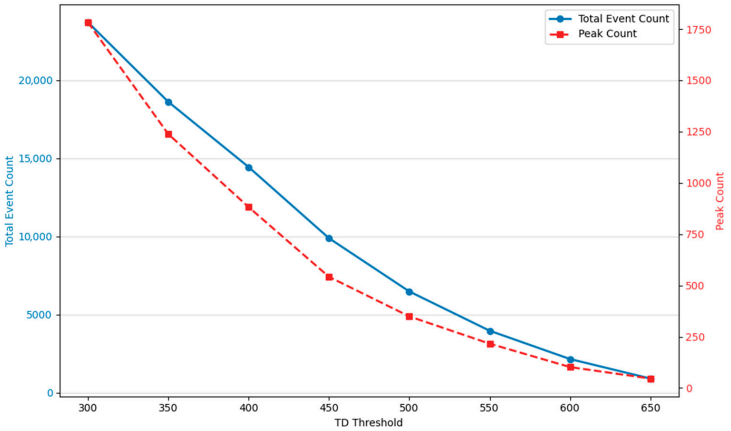


Figure 5. Quantitative relationship between TD threshold and event count metrics.

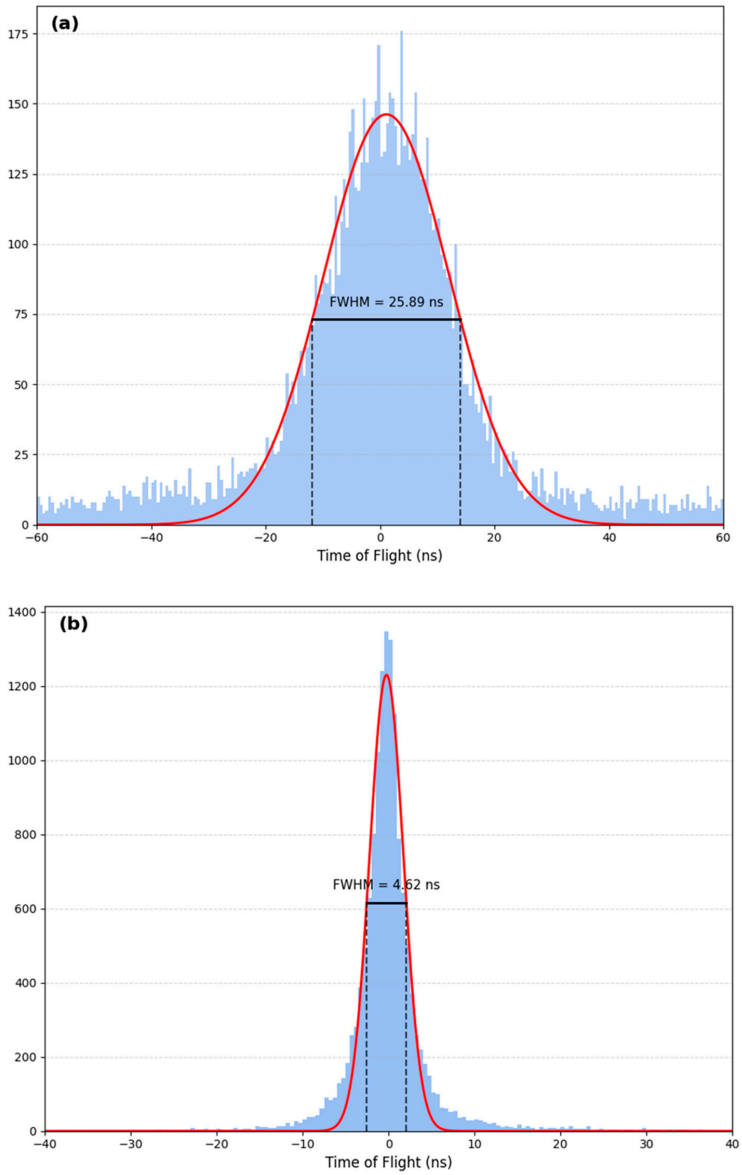


Figure 6. ToF histograms obtained at (**a**) TD threshold = 0 and (**b**) TD threshold = 300 conditions.

Performance validation was conducted using Cs-137 source measurements at 20 random positions distributed throughout the measurement area. Figure 7 illustrates the spatial distribution of the data points where the blue dots represent the 45 training grid

positions spaced at 25 cm intervals while the red dots indicate the 20 random test positions. As shown, the test points are located in the inter-grid gaps serving as unseen data to evaluate the spatial interpolation capability of the model. To illustrate the signal characteristics obtained at these off-grid locations Figure 8 presents time difference histograms for four representative test positions with panels a and b corresponding to the *X*-axis and *Y*-axis sensor measurements, respectively. The histograms show source position dependence with varying peak locations corresponding to different ToF values. The numbers in the legend represent the total event count detected by each individual fiber channel. Multiple peaks observed in the histograms arise from the U-shaped fiber topology, where a single fiber traverses the measurement area twice, and from simultaneous detection by adjacent fibers. In this context, the highest-peak selection logic isolates the dominant signal cluster corresponding to the unique source position.

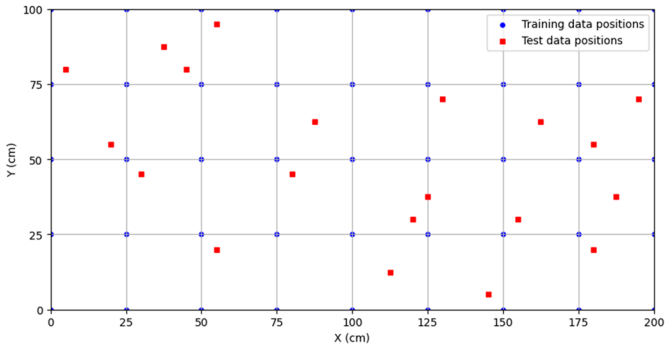


Figure 7. Data points where blue dots represent training data positions and red dots represent test data positions.

Table 2 details the accuracy improvement rates calculated using Equation (4), comparing the ANN model estimation to the theoretical calculation for the 20 random test positions. The mean FSE was reduced from 22.5% for the theoretical calculation to 4.6% for the ANN-based model. The mean accuracy improvement rate averaged across all 20 random test positions was 79.34%. Improvement rates ranged from 31.36% to 96.77% depending on the specific position.

Table 2. FSE and accuracy improvement rate comparison for theoretical and ANN-based position estimation.

Actual Position (cm, cm)	Ann Model FSE (%)	Theoretical FSE (%)	Improvement Ratio (%)
(5, 80)	1.1	34.1	96.77
(20, 55)	7.7	24.5	68.57
(30, 45)	6.4	23.9	73.22
(37.5, 87.5)	8.1	11.8	31.36
(45, 80)	5.3	14.3	62.94
(55, 20)	6.2	12.5	50.40
(55, 95)	7.6	15.3	50.33
(80, 45)	3.4	6.3	46.03
(87.5, 62.5)	1.7	4.7	63.83
(112.5, 12.5)	1.6	19.3	91.71
(120, 30)	4.0	22.6	82.30
(125, 37.5)	5.9	29.9	80.27
(130, 70)	5.3	20.3	73.89
(145, 5)	2.6	18.8	86.17
(155, 30)	7.3	25.8	71.71
(162.5, 62.5)	2.7	34.1	92.08
(180, 20)	2.7	35.3	92.35

Table 2. *Cont.*

Actual Position (cm, cm)	Ann Model FSE (%)	Theoretical FSE (%)	Improvement Ratio (%)
(180, 55)	5.5	34.1	83.87
(187.5, 37.5)	2.3	31.2	92.63
(195, 70)	5.4	30.4	82.24
Average	4.6	22.5	79.34

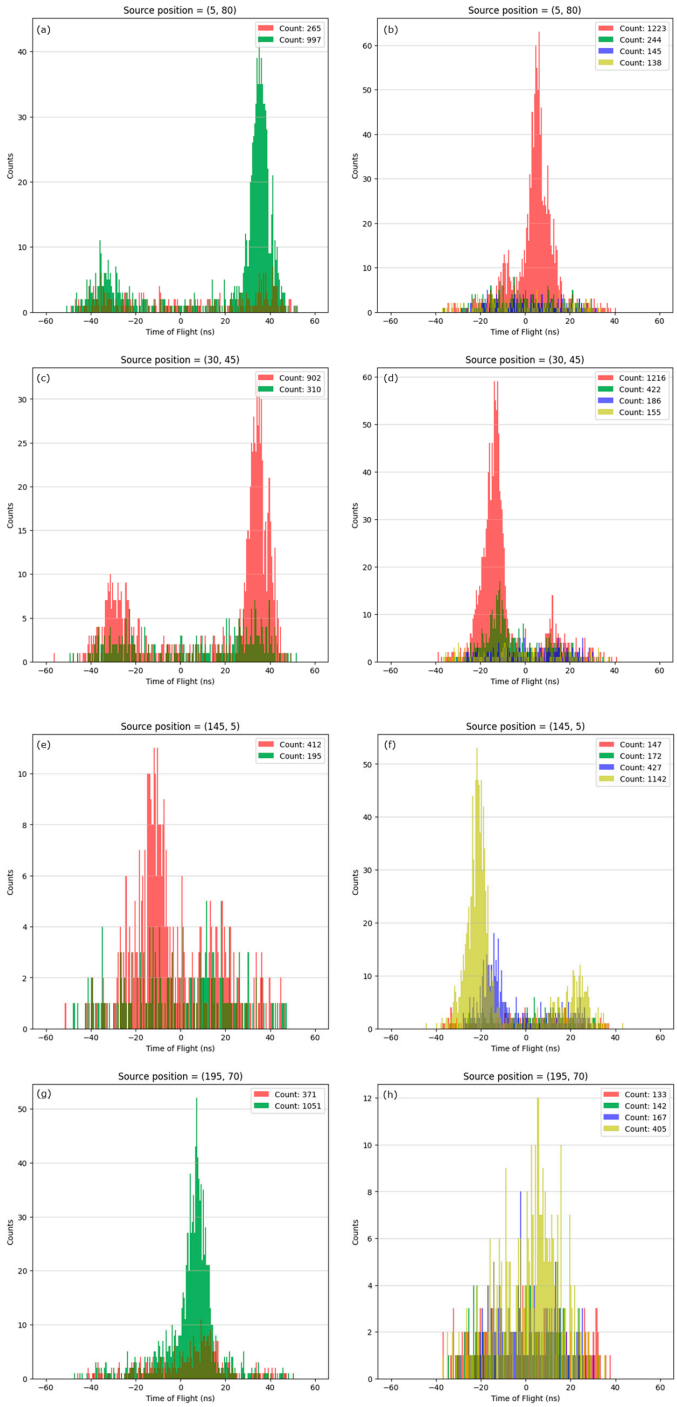


Figure 8. Time difference histograms for representative test positions. The plots correspond to (5, 80) (**a**,**b**), (30, 45) (**c**,**d**), (145, 5) (**e**,**f**), and (195, 70) (**g**,**h**). In each pair, the first and second labels represent the *X*-axis and *Y*-axis sensor measurements, respectively. The different colors represent data from individual sensors.

To evaluate measurement precision, nine repeated measurements were conducted at a fixed position with coordinates (95 cm, 45 cm) using the Cs-137 source. Table 3 presents the ANN model position estimation errors for the nine repeated measurements. *X*-axis errors ranged from −7.22 cm to −6.06 cm, *Y*-axis errors ranged from −2.66 cm to −1.74 cm, and 2D position errors ranged from 6.46 cm to 7.43 cm. The overall 2D standard deviation, calculated using the root-sum-square method from the standard deviations of both axes, measured 0.492 cm.

Table 3. ANN model Localization error for repeated measurements and standard deviations.

	X-Axis Estimation Error (cm)	Y-Axis Estimation Error (cm)	2D Euclidean Error (cm)
#1	−6.44	−2.41	6.88
#2	−7.22	−1.74	7.43
#3	−6.73	−2.34	7.12
#4	−6.94	−2.36	7.33
#5	−6.11	−2.34	6.54
#6	−6.09	−2.66	6.65
#7	−6.76	−2.47	7.19
#8	−6.76	−2.03	7.05
#9	−6.06	−2.22	6.46
Standard deviation (cm)	0.413	0.267	0.492

4. Discussion

This study demonstrated a 2D gamma-ray source localization system utilizing a mesh-based PSF array with Silicon Photomultiplier readout and ANN analysis. The system yielded a mean FSE of 4.6% across 20 random test positions. The U-shaped fiber topology allowed for one readout per spatial axis, reducing the required data acquisition hardware while providing 2D coverage.

The ANN method addressed systematic deviations in ToF measurements. Unlike theoretical calculations that assume uniform light propagation and constant timing offsets, the experimental setup is subject to position-dependent errors caused by light attenuation and channel-to-channel timing variations. Following the methodology established in our previous work [14], the two-stage training process compensated for these non-linear biases. The reduction in mean FSE by 79.34% compared to the theoretical calculation indicates that the neural network mapped the time-position relationship for the SiPM-based readout system.

This study is subject to specific constraints regarding its operational scope and long-term stability. First, experimental validation was strictly defined for surface contamination monitoring, with radioactive sources placed on the detector plane. This configuration aligns with the intended objective of mapping 2D surface distributions. Second, PSFs are susceptible to optical degradation over time due to oxidation or radiation exposure. Such aging effects alter attenuation characteristics and affect model accuracy. For practical deployment, a periodic re-calibration protocol using a reference source is required to update model parameters.

Future research will address system extension to complex monitoring scenarios. The current system employs a dominant signal selection strategy optimized for locating a single radioactive source. In scenarios involving multiple simultaneous sources, time difference histograms exhibit overlapping peaks that are not resolved by the current logic. Extending the system to multi-source localization requires restructuring the data processing pipeline to include pre-classification algorithms and neural network architectures capable of variable outputs. Multi-source separation and three-dimensional volumetric tracking are identified as subjects for future research.

Author Contributions: Conceptualization, J.K.; methodology, J.K. and S.L.; software, J.K.; validation, J.K., J.H.P. and S.K.; formal analysis, J.K.; investigation, B.L.; resources, J.K.; data curation, J.K. and S.L.; writing—original draft preparation, J.K.; writing—review and editing, J.K., C.H. and B.L.; visualization, J.K.; supervision, S.H.C. and B.L.; project administration, B.L.; funding acquisition, B.L. All authors have read and agreed to the published version of the manuscript.

Funding: This research was supported by the National Research Foundation of Korea (NRF) grant funded by the Korean government (MSIT) (No. 2020M2D2A2062457), and Korea Institute of Energy Technology Evaluation and Planning (KETEP) grant funded by the Ministry of Trade, Industry and Energy (MOTIE) of Republic of Korea (grant number RS-2024-00398867).

Data Availability Statement: The original contributions presented in this study are included in the article. Further inquiries can be directed to the corresponding author.

Conflicts of Interest: The authors declare no conflicts of interest.

Abbreviations

The following abbreviations are used in this manuscript:

INES	International nuclear and radiological event scale
PSF	Plastic scintillating fiber
ToF	Time-of-flight
ANN	Artificial neural network
1D/2D	One-dimensional/Two-dimensional
PMT	Photomultiplier tube
SiPM	Silicon photomultiplier
ReLU	Rectified linear unit
TD	Time discriminator
FSE	Full-scale error
ToT	Time-over-threshold
ADU	Arbitrary digital units

References

1. International Atomic Energy Agency (IAEA). *Environmental Consequences of the Chernobyl Accident and Their Remediation: Twenty Years of Experience, Report of the UN Chernobyl Forum Expert Group "Environment"*; Radiological Assessment Reports Series; IAEA: Vienna, Austria, 2006.
2. International Atomic Energy Agency (IAEA). *The Fukushima Daiichi Accident: Report by the Director General*; STI/PUB/1710; IAEA: Vienna, Austria, 2015.
3. International Atomic Energy Agency (IAEA). *The International Nuclear and Radiological Event Scale (INES) User's Manual*, 2008 ed.; IAEA: Vienna, Austria, 2013.
4. International Commission on Radiological Protection (ICRP). Radiological Protection in Medicine; ICRP Publication 105. *Ann. ICRP* **2007**, *37*, 6.
5. Knoll, G.F. *Radiation Detection and Measurement*, 4th ed.; John Wiley & Sons: New York, NY, USA, 2010.
6. Saint-Gobain Crystals. Organic Scintillation Materials and Assemblies. Available online: https://luxiumsolutions.com/sites/default/files/2021-12/Organics-Plastic-Scintillators.pdf (accessed on 1 November 2025).
7. Kuraray Co., Ltd. *Plastic Scintillating Fibers General Technical Information*; Kuraray Co., Ltd.: Tokyo, Japan, 2019.
8. U.S. Environmental Protection Agency. *Plastic Scintillation Fibers for Radiological Contamination Surveys*; EPA/600/R-17/370; U.S. EPA: Washington, DC, USA, 2017.
9. Klanner, R. Characterisation of SiPMs. *Nucl. Instrum. Methods Phys. Res. Sect. A* **2019**, *926*, 36–56. [CrossRef]
10. Goodfellow, I.; Bengio, Y.; Courville, A. *Deep Learning*; MIT Press: Cambridge, MA, USA, 2016.
11. Arridge, S.; Maass, P.; Öktem, O.; Schönlieb, C.B. Solving inverse problems using data-driven models. *Acta Numer.* **2019**, *28*, 1–174. [CrossRef]
12. Shimazoe, K.; Takahashi, H. Development of simultaneous PET and Compton imaging using GAGG-SiPM based pixel detectors. *Nucl. Instrum. Methods Phys. Res. Sect. A* **2020**, *954*, 161499. [CrossRef]
13. Bom, V.; van Roosmalen, J.; Venema, L. Neural networks and Gamma-ray spectroscopy. *Nucl. Instrum. Methods Phys. Res. Sect. A* **1995**, *356*, 322–326.

14. Kim, J.; Song, S.; Park, J.H.; Kim, S.; Lee, S.; Cho, S.H.; Huh, C.; Lee, B. Time-of-flight based one-dimensional position estimation of radioactive sources using artificial neural network model. *N. Eng. Technol.* **2025**, *57*, 103662. [CrossRef]
15. Piemonte, C.; Gola, A. Overview on the main parameters and technology of modern Silicon Photomultipliers. *Nucl. Instrum. Methods Phys. Res. Sect. A* **2019**, *926*, 2–15. [CrossRef]
16. Acerbi, F.; Gundacker, S. Understanding and simulating SiPMs. *Nucl. Instrum. Methods Phys. Res. Sect. A* **2019**, *926*, 16–35. [CrossRef]
17. Gundacker, S.; Turtos, R.M.; Kratochwil, N.; Pots, R.H.; Paganoni, M.; Lecoq, P.; Auffray, E. Experimental time resolution limits of modern SiPMs and TOF-PET detectors exploring different scintillators and Cherenkov emission. *Phys. Med. Biol.* **2020**, *65*, 025001. [CrossRef] [PubMed]
18. Onsemi (Formerly SensL Technologies). *ARRAYJ-60035-64P-PCB Silicon Photomultiplier Array Datasheet*; Onsemi: Scottsdale, AZ, USA, 2018.
19. CAEN S.p.A. *DT5202 Desktop Digitizer User Manual, Rev. 4*; CAEN S.p.A.: Viareggio, Italy, 2020.
20. CAEN S.p.A. *DT5215 Data Concentrator Module User Manual, Rev. 1*; CAEN S.p.A.: Viareggio, Italy, 2020.
21. Kingma, D.P.; Ba, J. Adam: A method for stochastic optimization. In Proceedings of the 3rd International Conference on Learning Representations (ICLR), San Diego, CA, USA, 7–9 May 2015.

Disclaimer/Publisher's Note: The statements, opinions and data contained in all publications are solely those of the individual author(s) and contributor(s) and not of MDPI and/or the editor(s). MDPI and/or the editor(s) disclaim responsibility for any injury to people or property resulting from any ideas, methods, instructions or products referred to in the content.